Supporting Information

1. Materials

Fluorine doped tin oxide (FTO, Nippon Sheet Glass, Japan, 2.2 mm thick, 14 Ω) substrates were purchased from Wu Han Jinge-solar Energy Technology Co., Ltd. The FTO glasses were sonicated sequentially in acetone, ethanol, and distilled water for 30 minutes, respectively. Indium trichloride ($InCl_3$, metals basis, 99.99%), bismuth chloride ($BiCl_3$, AR, ≥ 99%), thioacetamide (CH_3CSNH_2, metals basis, 99.999%), ethylene glycol ($(CH_2OH)_2$, AR, 99.9%), sodium sulfate (Na_2SO_4, AR, 99.5%), and sodium sulphite (Na_2SO_3, AR, 99.5%) were purchased from Aladdin and all chemicals were used without any further purification. Deionized water was used for preparation of solutions and washing.

2. Physical characterization

The X-ray diffraction (XRD) was detected on a Shimadzu ZD-3AX diffractometer with Cu Kα radiation (λ = 1.5418 Å). The 2θ scanning angular range was from 10° to 90° with rate of 2° per minute. Raman spectra of these samples were conducted by using LabRAM HR Evolution (λ_{exc} = 532 nm). The morphologies and high-resolution microstructure images were recorded though a field emission scanning electron microscope (FE-SEM, Nova 400 Nano-SEM) and transmission electron microscope (TEM, Talos F200S, 200kV). The surface composition and chemical state was carried out by the X-ray photoelectron spectroscopy (XPS, ESCALab250) technique, all spectra were calibrated by using the C 1s peak at 284.8 eV. The optical properties of as-prepared samples were performed by a spectrophotometer (UV-3600, Shimadzu) in the region of 300 - 900 nm, room temperature photoluminescence (PL) measurement were carried out with a fluorescence spectrometer (Cary eclipse) with an excitation wavelength of 365 nm; the measured powder was scraped from the FTO substrate.

3. Photoelectrochemical measurements

Electrochemical tests were carried out by using a Zahner Zennium electrochemical workstation (Zennium and PP211, Germany) in a standard three-electrode configuration, a photoanode (1 cm^2) used as the working electrode. Meanwhile, a Pt coil (diameter is about 1 mm, length is about 5 cm) served as the counter electrode, an Ag/AgCl electrode (saturated KCl) used as the reference electrode. The photo-response of the synthesized electrodes were measured under front-side illumination by a 300 W Xenon arc lamp (NBet HSX-F300, China) equipped with an AM 1.5G filter (Ceaulight). The intensity of the light source was calibrated with a UV enhanced silicon photo-detector (Newport, Models 1916C and 818-UV) to simulate one solar illumination (100 mW cm^{-2}). The applied potential versus Ag/AgCl was converted to RHE by the Nernst equation:

$$E_{RHE} = E_{Ag/AgCl} + 0.0591\ pH + E^{\circ}_{Ag/AgCl} \quad (1)$$

$E^{\circ}_{Ag/AgCl}$ is 0.1976 V vs. RHE at 25 °C. In a typical experiment, 0.2 M Na_2SO_4 (pH 6.8) with/without 0.5 M Na_2SO_3 as a hole scavenger was used as the electrolyte. For all samples, a positive scan rate of 25 mV s^{-1} was used for the photocurrent-voltage (*J*-V) measurements. Photocurrent stability tests were performed at a fixed bias potential of 0.90 V vs. RHE and the incident photo to current efficiency (IPCE) performance was performed at 1.23 V vs. RHE under illumination. The IPCE is expressed by the following equation:

$$IPCE = (J \times 1240) / (P_{light} \times \lambda) \quad (2)$$

where J is the measured photocurrent density at a specific wavelength (mA cm^{-2}), λ is the incident light wavelength (nm), and P_{light} is the recorded irradiance intensity at a specific wavelength (mW cm^{-2}). The photovoltages of various photoanodes were estimated by the onset potential (E) shift of the anodic current in dark and under illumination. The controlled intensity modulated photo spectroscopy (CIMPS) was conducted with the frequency range from 10k to 1 Hz with water oxidation, which was conducted by a constant power density (λ = 365 nm, 5 mW cm^{-2}) under different potential. The charge transport time (τ) could be calculated by the following equation,

$$\tau = 1 / 2\pi f \quad (3)$$

where τ and f are electron transport time across the film and the minimum characteristic frequency. Mott-Schottky plots were obtained in 0.2 M Na_2SO_4 at an ac frequency of 500 and 1000 Hz. The carrier concentration and the flat band potential can be estimated by the following equation:

$$(A_s / C_{bulk})^2 = (2 / e\varepsilon\varepsilon_0 N_d)[V - V_{fb} - k_B T / e] \quad (4)$$

where A_s is the efficient area of electrode, C_{bulk} is the space charge capacitance, ε is the dielectric constant of the samples, ε_0 is the permittivity under vacuum (8.85×10^{-12} $C^2 J^{-1} m^{-2}$). N_d is the carrier density of the samples, V is the applied potential, V_{fb} is the flat band potential, k_B is the Boltzmann constant (1.38×10^{-23} J K^{-1}), T (298 K) is the absolute temperature, and e is the electron charge (1.602×10^{-19} C).

4. Calculations for the efficiencies of charge separation and oxidation kinetics

The photocurrent density arising from PEC performance (J_{water}) can be described as follows:

$$J_{water} = J_{abs} \times \eta_{sep} \times \eta_{ox} \quad (5)$$

where J_{abs} is the photocurrent density when completely converting the absorbed photons into current (i.e., APCE = 100%). η_{sep} is the efficiency of charge separation and η_{ox} is the efficiency of surface oxidation kinetics. Adding 0.5 M Na_2SO_3 to the electrolyte can completely suppress the surface recombination of charge carriers without influencing the charge separation in the electrode bulk (i.e., η_{ox} = 100%). Therefore, η_{sep} and η_{ox} can be expressed as follows:

$$\eta_{sep} = J_{sulfite} / J_{abs} \quad (6)$$

$$\eta_{ox} = J_{water} / J_{sulfite} \quad (7)$$

where J_{water} is the photocurrent density for water oxidation; $J_{sulfite}$ is the photocurrent density for sulfite oxidation. By estimating the overlapped areas between the AM 1.5G illumination, assuming APCE = 100%, the J_{abs} of Bi_2S_3, In_2S_3, and $In_2S_3@Bi_2S_3$ photoanodes are derived to be around 5.6, 4.2, and 6.5 mA cm^{-2}.

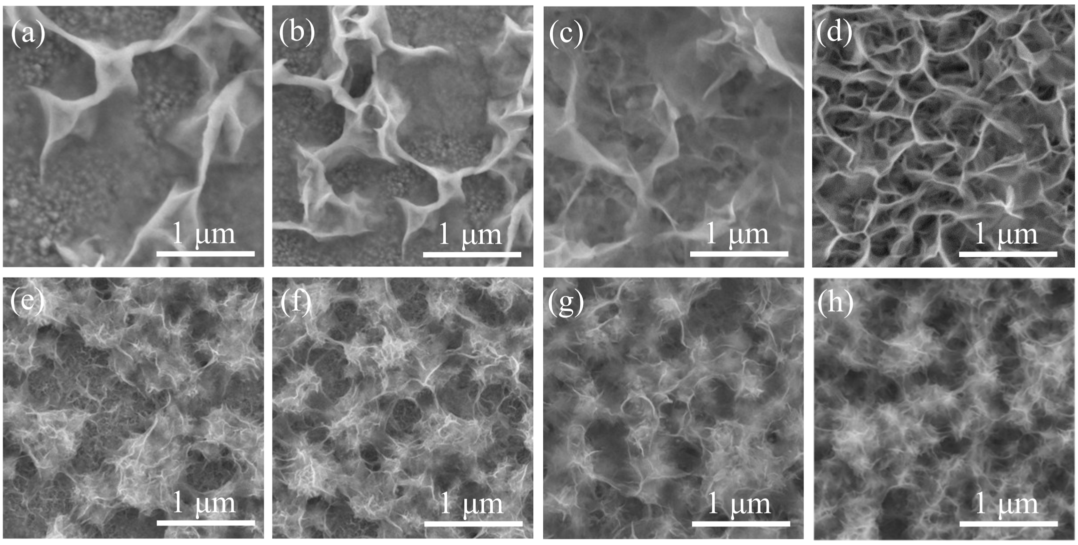

Fig. S1. SEM images of In_2S_3 synthesized by different concentrations of indium trichloride in ethylene glycol solvothermal process, including (a) 3 mM, (b) 6 mM, (c) 12 mM, and (d) 20 mM. SEM images of typical In_2S_3@Bi_2S_3 structures by using different concentrations of indium trichloride, including (e) 3 mM, (f) 6 mM, (g) 12 mM, and (h) 20 mM of indium trichloride. For the optimized structure of In_2S_3@Bi_2S_3, the inner layer Bi_2S_3 was fabricated by using 20 mM bismuth chloride and 35 mM thioacetamide, and then served as the substrate for growing the In_2S_3@Bi_2S_3 heterostructures.

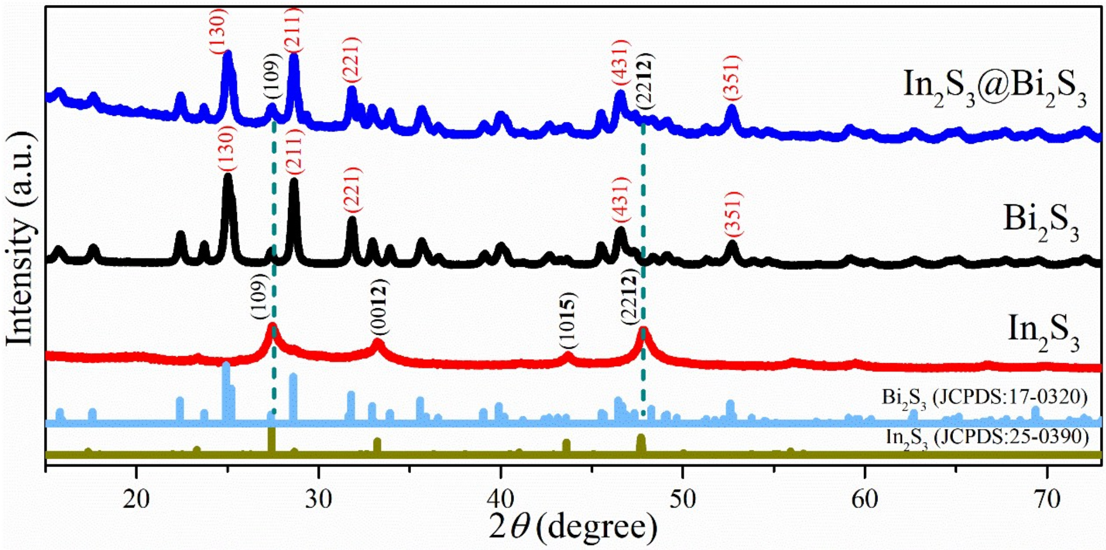

Fig. S2. The XRD patterns of In_2S_3, Bi_2S_3, and In_2S_3@Bi_2S_3. The mismatched lattice parameters of In_2S_3 (a = 7.691, b = 7.691, and c = 32.329 Å) and Bi_2S_3 (a = 11.149, b = 11.304, and c = 3.981 Å) in crystalline structure will lead to lattice strain when the two structures grow together. Moreover, the diffraction peaks situated at 24.93°, 28.61°, 31.79°, 46.46° and 52.62° are consistent with the planes of (130), (211), (221), (431), and (351) with Bi_2S_3, while the diffraction peaks located at 27.43°, 33.23°, 43.60°, and 47.70° agree well with the planes of (109), (00**12**), (10**15**), and (22**12**) by pure In_2S_3.

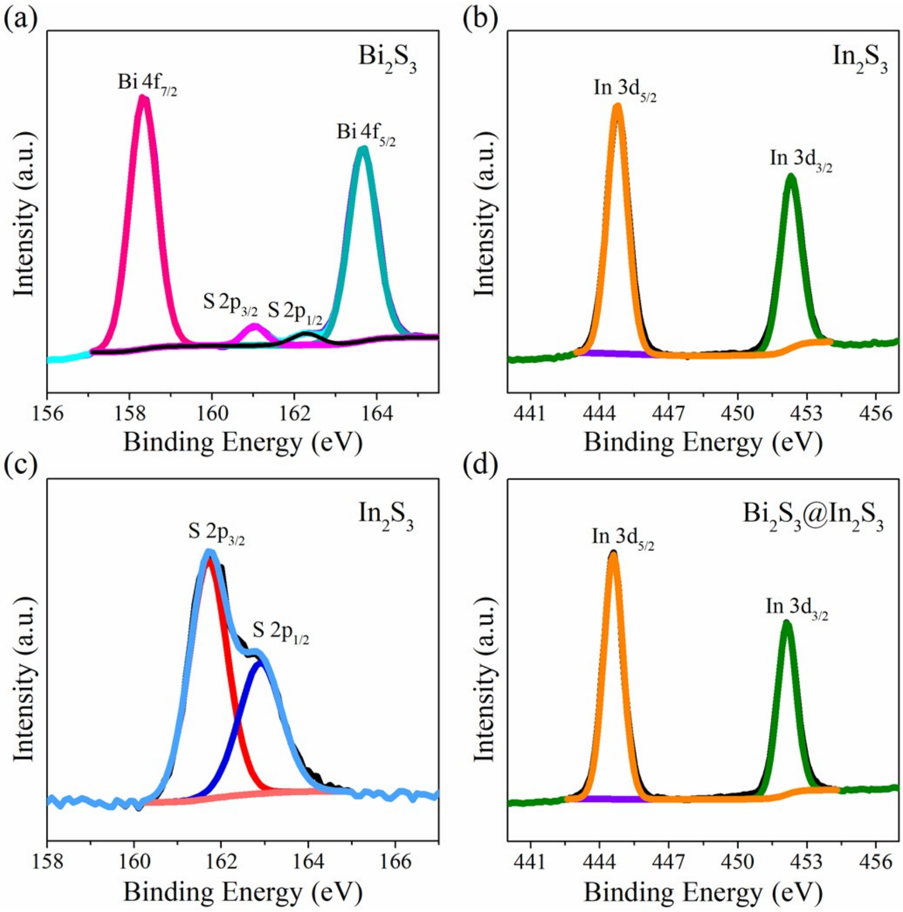

Fig. S3. XPS spectra of (a) Bi 4f and S 2p orbitals for Bi_2S_3, (b) In 3d and (c) S 2p orbitals for In_2S_3, and (d) the In 3d orbitals for In_2S_3@Bi_2S_3.

The characteristic Bi 4f$_{7/2}$ and Bi 4f$_{5/2}$ peaks appeared at 158.3 and 163.6 eV, which is consistent with the standard Bi^{3+} peaks of Bi_2S_3.[1] The signals located between Bi 4f$_{5/2}$ and Bi 4f$_{7/2}$ could be attributed to the S 2p$_{1/2}$ at 162.3 eV and the S 2p$_{3/2}$ at 161.1 eV. The In 3d$_{5/2}$ and In 3d$_{3/2}$ are located at 444.9 and 452.4 eV with a ΔE of 7.5 eV, demonstrating the typically In^{3+}. The two strong peaks at 161.7 and 162.9 eV are corresponding to the S 2p$_{3/2}$ and S 2p$_{1/2}$.[2] The In 3d spectrum consists of In 3d$_{5/2}$ (444.8 eV) and In 3d$_{3/2}$ (452.3 eV) for In_2S_3@Bi_2S_3. The lower binding energies of In^{3+} suggests the change of chemical bonding energy with interfacial electronic interaction in In_2S_3@Bi_2S_3 heterostructures.

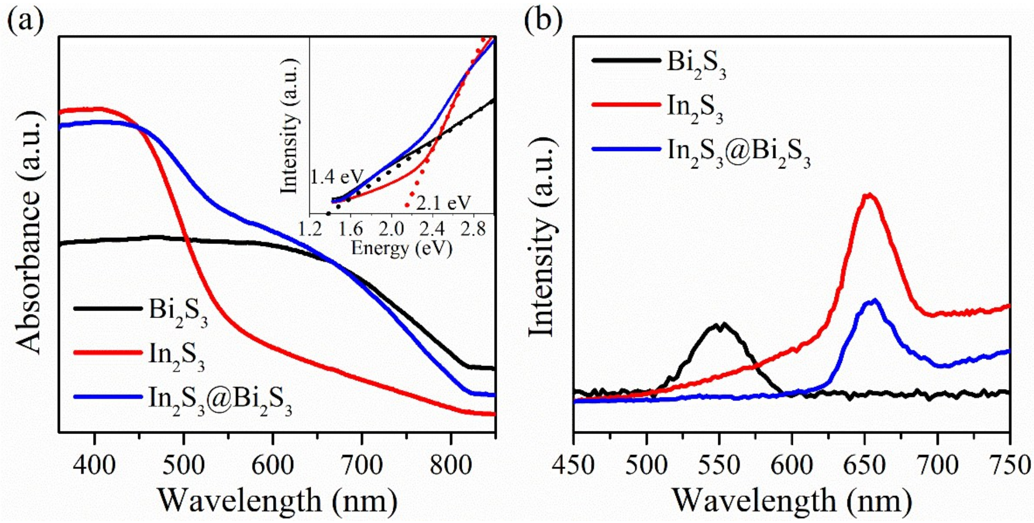

Fig. S4. (a) The UV-vis absorption spectra for Bi_2S_3, In_2S_3, and $In_2S_3@Bi_2S_3$, and the inset is the Tauc's plots of these semiconductors, indicating the bandgap of Bi_2S_3 and In_2S_3 is nearly 1.4 and 2.1 eV. The UV-vis absorption spectra reveal the absorption edge of $In_2S_3@Bi_2S_3$ heterostructure has a red-shift compared with In_2S_3 and Bi_2S_3. (b) The Photoluminescence (PL) spectra of different samples under excitation (λ_{ex} = 365 nm).

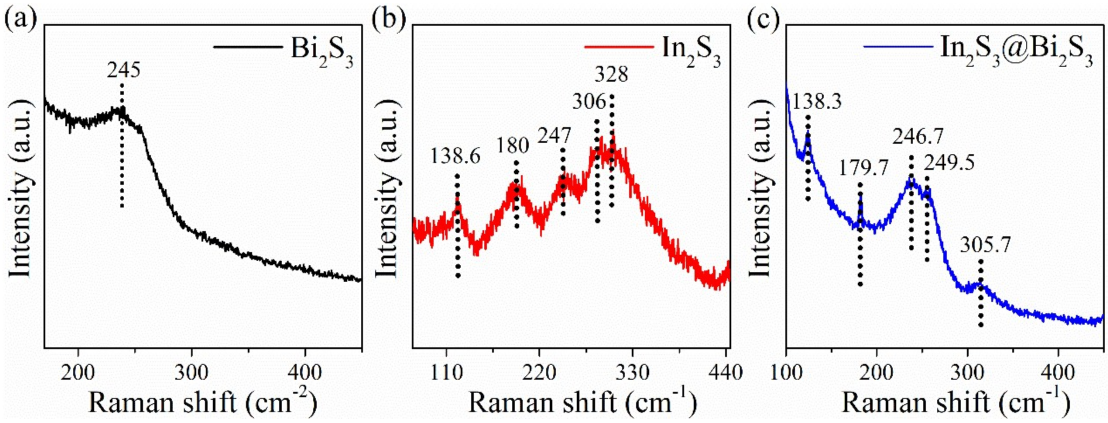

Fig. S5. Raman spectra of (a) bare Bi_2S_3, (b) bare In_2S_3, and (c) In_2S_3@Bi_2S_3 composite.

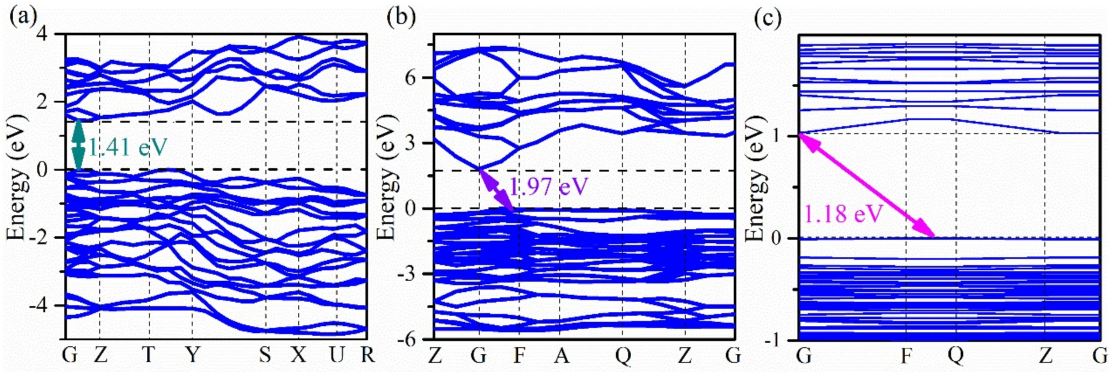

Fig. S6. The simulated band structure of (a) Bi_2S_3, (b) In_2S_3, and (c) In_2S_3@Bi_2S_3. In detail, Bi_2S_3 has a direct bandgap (1.41 eV) where the valance band maximum (VBM) and the conduction band minimum (CBM) both lie at general points between G and Z point. A large bandgap of 1.97 eV is observed for In_2S_3, where the VBM locates between G and F while the CBM locates at G point. Specifically, the slab model of In_2S_3 is obtained from the bulk structures on (001) direction with vacuum (10 Å), and the Bi_2S_3 (010) direction has been established with vacuum (10 Å).

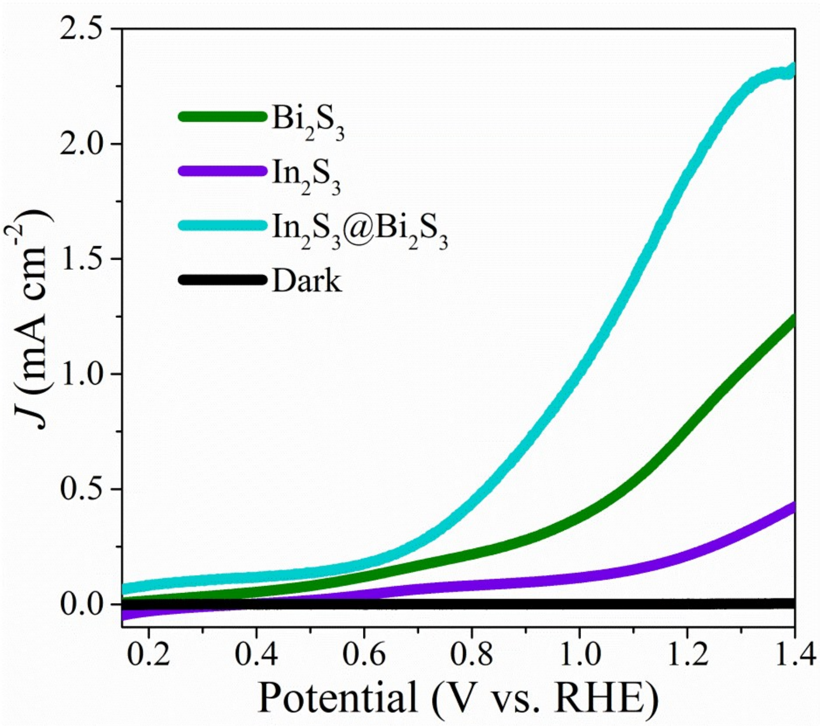

Fig. S7. *J*-V plots of various samples for sulfite oxidation in 0.2 M Na_2SO_4 with 0.5 M Na_2SO_3 under AM 1.5G illumination.

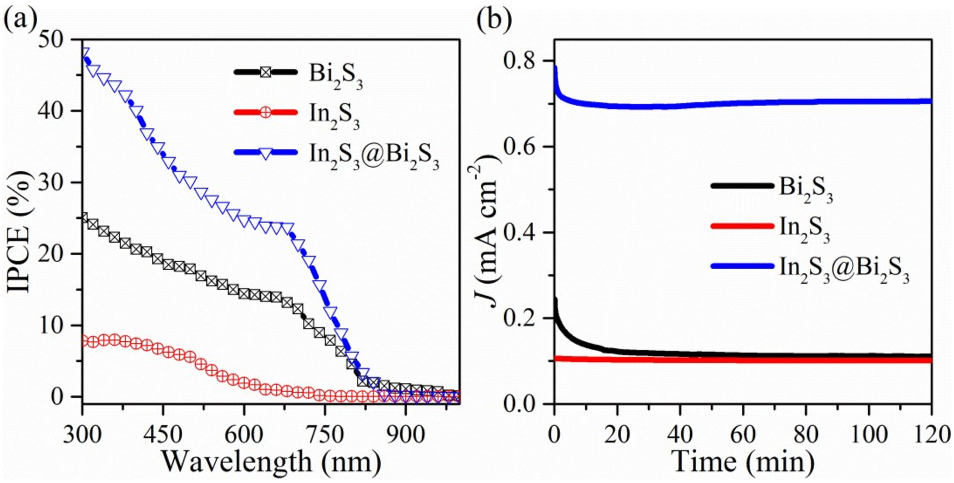

Fig. S8. (a) IPCE for different samples at 1.23 V vs. RHE, and (b) photocurrent density versus time at 0.9 V vs. RHE in 0.2 M Na_2SO_4 solution. The IPCE value of $In_2S_3@Bi_2S_3$ varies between 32%-45% at 500-350 nm and maintains a relative high value under broadband-light irradiation, suggesting the PEC performance of $In_2S_3@Bi_2S_3$ is higher than Bi_2S_3 nanorods and In_2S_3 nanosheets. During stability test for 2 hours, the results exhibit $In_2S_3@Bi_2S_3$ possess around 90% of its initial photocurrent, confirming the good stability of 2D/1D $In_2S_3@Bi_2S_3$ heterostructures under continuous water oxidation.

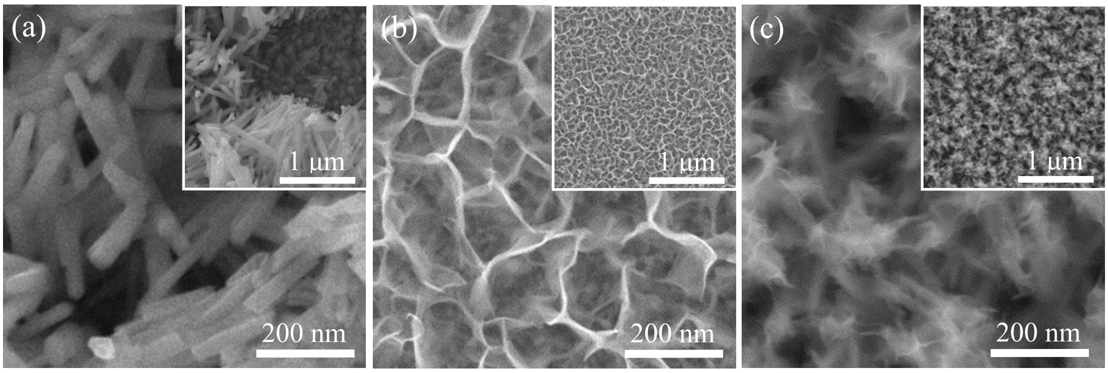

Fig. S9. SEM images of typical (a) Bi_2S_3 nanorods, (b) In_2S_3 nanosheets, and (c) In_2S_3@Bi_2S_3 heterostructure after stability test for 2 hours.

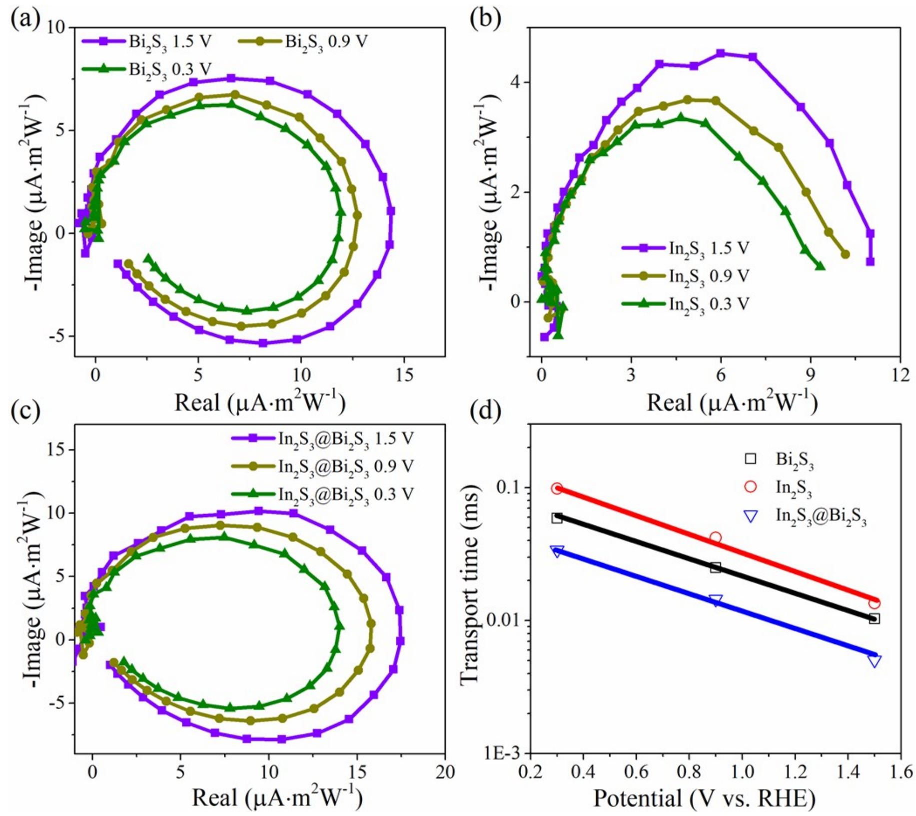

Fig. S10. Plots of CIMPS complex plane of (a) Bi_2S_3, (b) In_2S_3, and (c) In_2S_3@Bi_2S_3 with water oxidation at different applied potential (1.5, 0.9, and 0.3 V vs. RHE) with constant power density (5 mW cm^{-2}). (d) The electrons' transport time (τ) originated from CIMPS complex plane at different potential in 0.2 M Na_2SO_4 solution (pH 6.8).

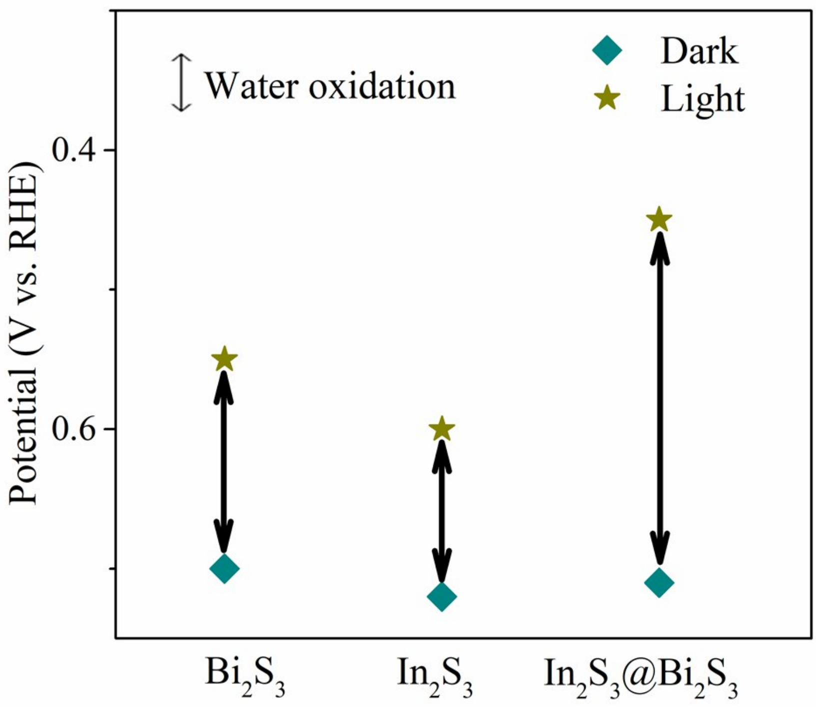

Fig. S11. The photovoltage (V_{ph}) for various photoanodes, which estimated by the onset potential (E) shift of anodic current in dark and under illumination. The V_{ph} could be written as: $V_{ph} = |E_{dark} - E_{light}|$.

Table S1 The PEC performances of In_2S_3-based compounds compared with this study.

Photocatalyst	Electrolyte	Applied bias	J (μA/cm^2) Original	J (μA/cm^2) Improved	Multiple	Ref
2D β-In_2S_3	---	1.0 V vs. NHE	0.03 (In_2S_3)	0.15 (In_2S_3)	5.0	2
In_2O_3/ In_2S_3/CdS	0.1 M Na_2SO_4	---	300 (In_2O_3/ In_2S)	700 (In_2O_3/ In_2S_3/CdS)	2.3	3
In_2O_{3-x}/In_2S_3	1.0 M KOH	1.4 V vs. NHE	137 (Pure In_2S_3)	1570 (In_2O_{3-x}/In_2S_3)	11.5	4
In_2S_3/MoS_2/CdS	0.1 M Na_2SO_4	---	25 (In_2S_3/CdS)	250 (In_2S_3/MoS_2/ CdS)	10	5
In_2S_3-CNT	0.2 M Na_2SO_4	---	0.7 Blank In_2S_3	1.1 (In_2S_3-CNT)	1.6	6
Titania@β-In_2S_3	0.25 M Na_2S and 0.35 M Na_2SO_3	0.4 V vs. Ag/AgCl	800 1-TiO_2@In_2S_3	1400 2-TiO_2@In_2S_3	1.75	7
MoS_2@In_2S_3	0.2 M Na_2S and Na_2SO_3	0.2 V vs. SCE	0.3	1.0 MoS_2@In_2S_3	3.3	8
In_2S_3/Anatase/Rutile TiO_2	0.3 M Na_2SO_4	1.23 V vs. RHE	1350 ANP/RND	1550 In_2S_3/ANP/RNP	1.2	9
In_2S_3@MCPAs	1.0 M KCl	1.23 V vs. RHE	7.2 In_2S_3@Planar	25.7 In_2S_3@MCPA	3.6	10
In_2S_3@Bi_2S_3	0.2 M Na_2SO_4	1.23 V vs. RHE	**150** (Pure In_2S_3)	**2000**	**13.3**	**This work**

Notes and references

1 P. Li, X. Zhang, C. Hou, Y. Chen and T. He, *Appl. Catal. B-Environ.*, 2018, **238**, 656-663.

2 W. Huang, L. Gan, H. Yang, N. Zhou, R. Wang, W. Wu, H. Li, Y. Ma, H. Zeng and T. Zhai, *Adv. Funct. Mater.*, 2017, **27**, 1702448.

3 Y. Xiao, G. Tian, Y. Chen, X. Zhang, H. Fu and H. Fu, *Appl. Catal. B-Environ.*, 2018, **225**, 477-486.

4 J. Hou, S. Cao, Y. Sun, Y. Wu, F. Liang, Z. Lin and L. Sun, *Adv. Energy Mater.*, 2018, **8**, 170114.

5 W. Jiang, Y. Liu, R. Zong, Z. Li, W. Yao and Y. Zhu, *J. Mater. Chem. A*, 2015, **3**, 18406-18012.

6 M. Q. Yang, B. Weng and Y. J. Xu, *J. Mater. Chem. A*, 2014, **2**, 1710-1720.

7 A. Mumtaz, N. M. Mohamed, M. Mazhar, M. A. Ehsan and M. S. Mohamed Saheed, *ACS Appl. Mater. Interfaces*, 2016, **8**, 9037-9049.

8 F. Liu, Y. Jiang, J. Yang, M. Hao, Z. Tong, L. Jiang and Z. Wu, *Chem. Commun.*, 2016, **52**, 1867-1870.

9 J. S. Yang and J. J. Wu, *ACS Appl. Mater. Interfaces*, 2018, **10**, 3714-3722.

10 M. Li, L. Chen, C. Zhou, C. Jin, Y. Su and Y. Zhang, *Nanoscale*, 2019, **11**, 18071-18080.